

the descending edge correspond to a negative chirp.

3.3.4 The SFA model

While the direct numerical integration of the TDSE provides the most accurate results, to achieve a much greater physical transparency we may turn instead to an alternate technique which began with the work of Lewenstein in 1994 [61]. This approach is based upon invoking the SFA (see §2.5.5), where an electron may only exist as bound within the field-free ground state of an atomic potential or as a Volkov function in the continuum, evolving solely under the influence of a laser field. The electronic wavefunction at some time t may thus be expressed by the sum

$$|\Psi(t)\rangle = a(t)|\psi_0\rangle e^{iI_p t} + \int_{\mathbf{p}} M_{\mathbf{p}}(t) |\chi_{\mathbf{p}}(t)\rangle d^3\mathbf{p} \quad (3.55)$$

where the ground state evolves as $|\psi(t)\rangle = |\psi_0\rangle e^{iI_p t}$ and with a population $a(t)$. The Volkov wave $|\chi_{\mathbf{p}}(t)\rangle$ is given by equations 2.81 and 2.83, and has a population given by the coefficient $M_{\mathbf{p}}(t)$ of equation 2.84. As previously \mathbf{p} represents the canonical momentum, expressed here in terms of kinetic momentum \mathbf{p}_K as

$$\mathbf{p} = \mathbf{p}_K(t) - \mathbf{A}(t) = \mathbf{p}_K(t') - \mathbf{A}(t') \quad (3.56)$$

Before proceeding we will point out some of the failings of applying the SFA here and their consequences.

1. The SFA is only the first term in the full *S-matrix* perturbative expansion with respect to atomic potential. This series does not in general converge.
2. The SFA is not gauge invariant. The length and velocity gauges will, for example, yield a different prefactor to the dipole moment as calculated below (see equations 3.57 and 3.70). This prohibits the theory from providing a correct absolute spectral amplitude, giving only relative values. Absolute amplitude may be recovered from a comparison with TDSE calculations, if feasible.
3. Ionisation amplitudes are incorrect as they neglect the core beyond the unperturbed ground state.
4. Continuum excursion is incorrect as it neglects the influence of the Coulomb potential.
5. The set of Volkov states is a complete basis, non-orthogonal to the initial bound state. This results in an overcomplete basis set which yields further inaccuracies in the prefactor.

In spite of these faults, the SFA is found to yield an accurate representation of the physics of HHG at energies exceeding the ionisation potential of the initial bound state.

Returning to equation 3.55, the electron's dipole moment may be calculated as

$$\begin{aligned}
\mathcal{D}(t) &= \langle \Psi(t) | \hat{\mathbf{r}} | \Psi(t) \rangle \\
&= \int_{\mathbf{p}} a^*(t) \mathbf{d}^*(\mathbf{p} + \mathbf{A}(t)) M_{\mathbf{p}}(t) e^{-i(I_p t + S_{\mathbf{p}}(t))} d^3 \mathbf{p} + c.c. \\
&= -i \int_{-\infty}^t \int_{\mathbf{p}} a^*(t) \mathbf{d}^*(\mathbf{p} + \mathbf{A}(t)) a(t') \mathbf{E}(t') \cdot \mathbf{d}(\mathbf{p} + \mathbf{A}(t')) e^{-iS_{\mathbf{p}}(t, t')} d^3 \mathbf{p} dt' + c.c.
\end{aligned} \tag{3.57}$$

where *c.c.* denotes complex conjugate and the classical action from t' to t is

$$S_{\mathbf{p}}(t, t') = I_p(t - t') + \frac{1}{2} \int_{t'}^t (\mathbf{p} + \mathbf{A}(t''))^2 dt'' \tag{3.58}$$

We have used the fact that the ground state is centred at the origin and there is no contribution from continuum-continuum transitions, i.e. $\langle \psi_0 | \hat{\mathbf{r}} | \psi_0 \rangle = \langle \mathbf{p} | \hat{\mathbf{r}} | \mathbf{p}' \rangle = 0$. We have also introduced the dipole transition matrix elements (DTMEs), $\mathbf{d}(\mathbf{p}) = \langle \mathbf{p} | \hat{\mathbf{r}} | \psi_0 \rangle$, to describe the transitions between the ground and Volkov states. By equation 2.82, these may be expressed in terms of the bound state momentum distribution, $\hat{\psi}_0(\mathbf{p})$, as

$$\begin{aligned}
\mathbf{d}(\mathbf{p}) &= \frac{1}{(2\pi)^{3/2}} \int_{-\infty}^{\infty} e^{-i\mathbf{p} \cdot \mathbf{r}} \mathbf{r} \psi_0(\mathbf{r}) d^3 \mathbf{r} \\
&= i \partial_{\mathbf{p}} \hat{\psi}_0(\mathbf{p})
\end{aligned} \tag{3.59}$$

From a computational perspective, note that the conjugate momentum \mathbf{p} is constant with time for a particular (t, t') pair and the vector potential $\mathbf{A}(t)$ is independent of these integration limits. By expressing the kinetic momentum in equation 3.57 as the sum of these two quantities we may thus significantly reduce the amount of data to be stored in this calculation.

By using the identity

$$\mathcal{F}\{\ddot{D}(t)\}(\omega) = -\omega^2 \mathcal{F}\{D(t)\}(\omega) \quad \text{for } \lim_{t \rightarrow \pm\infty} D(t) = 0 \tag{3.60}$$

where $\mathcal{F}\{\cdot\}$ denotes Fourier transform, the spectral amplitude of the dipole acceleration $\ddot{D}(t)$ along a polarisation axis $\hat{\mathbf{e}}$ is obtained from equation 3.57 as

$$\begin{aligned}
M_{\hat{\mathbf{e}}}(\omega) &= \frac{i\omega^2}{\sqrt{2\pi}} \int_{-\infty}^{\infty} \int_{-\infty}^t \int_{\mathbf{p}} a^*(t) \hat{\mathbf{e}} \cdot \mathbf{d}^*(\mathbf{p} + \mathbf{A}(t)) \\
&\times a(t') \mathbf{E}(t') \cdot \mathbf{d}(\mathbf{p} + \mathbf{A}(t')) e^{-iS_{\mathbf{p}, \omega}(t, t')} d^3 \mathbf{p} dt' dt + c.c.
\end{aligned} \tag{3.61}$$

where $S_{\mathbf{p},\omega}(t, t') = S_{\mathbf{p}}(t, t') + \omega t$. The radiated field may then be calculated by equations 3.4 and 3.7.

Physically, equations 3.57 and 3.61 define a three-step process akin to that described in §3.1.

1. Ionisation

The electron is initially bound in the unperturbed ground state $|\psi_0\rangle$ with energy $-I_p$. At time t' it escapes into a continuum state $|\chi_{\mathbf{p}}(t)\rangle$ with kinetic momentum $\mathbf{p} + \mathbf{A}(t')$. The action associated with the bound electron is $S^{(1)}(t') = -\int_{-\infty}^{t'} I_p dt''$ and the transition amplitude for the ionisation $a(t')\mathbf{E}(t') \cdot \mathbf{d}(\mathbf{p} + \mathbf{A}(t'))$.

2. Acceleration

The electron then evolves in the continuum according to equations 3.12–3.14 and the atomic potential is ignored. The associated action is $S_{\mathbf{p}}^{(2)}(t, t') = \frac{1}{2} \int_{t'}^t (\mathbf{p} + \mathbf{A}(t''))^2 dt''$.

3. Recollision

At time t , the electron recombines into the unperturbed ground state with a transition amplitude $a^*(t)\mathbf{d}^*(\mathbf{p} + \mathbf{A}(t))$. It then remains bound with energy $-I_p$ and associated action $S^{(3)}(t) = -\int_t^{\infty} I_p dt''$.

The action $S_{\mathbf{p}}(t, t')$ of equation 3.58 is then recovered by summing $S^{(1,2,3)}$ up to a global phase factor (this in fact calculates the difference from an electron bound in $|\psi_0\rangle$ for all time).

For a Hydrogenic orbital, we may calculate the DTMEs of equation 3.59 via the analytic expression for the bound state momentum distribution as provided by Podolsky and Pauling in 1929 [67]. Expressed in polar coordinates, (p, θ, ϕ) , this is

$$\hat{\phi}_0^{(nlm)}(p, \theta, \phi) = -Y_l^m(\theta, \phi) \frac{(-i)^l \pi 2^{2l+4} l!}{(2\pi\gamma)^{3/2}} \sqrt{\frac{n(n-l-1)!}{(n+l)!}} \frac{\zeta^l}{(\zeta^2+1)^{l+2}} C_{n-l-1}^{l+1} \left(\frac{\zeta^2-1}{\zeta^2+1} \right) \quad (3.62)$$

where (n, l, m) are the principle, azimuthal and magnetic quantum numbers of the bound state, $\gamma = Z_{\text{eff}}/n = \sqrt{2I_p}$ and $\zeta = p/\gamma$. $Y_l^m(\theta, \phi)$ are the spherical harmonics and $C_n^{(\lambda)}(x)$ are the Gegenbauer polynomials.

In the simplest case of a 1s hydrogenic orbital, equation 3.62 reduces to

$$\hat{\phi}_0^{(100)}(\mathbf{p}) = -\frac{2\sqrt{2\gamma^5}}{\pi(|\mathbf{p}|^2 + \gamma^2)^2} \quad (3.63)$$

with corresponding DTME given by equation 3.59 as

$$\mathbf{d}^{(100)}(\mathbf{p}) = i\partial_{\mathbf{p}} \hat{\phi}_0^{(100)}(\mathbf{p}) = \frac{i8\sqrt{2\gamma^5}\mathbf{p}}{\pi(|\mathbf{p}|^2 + \gamma^2)^3} \quad (3.64)$$

Comparing equation 3.58 with, for example, equation 3.64 illustrates that the action term in equation 3.57 has a much greater dependency on \mathbf{p} than does the DTME $\mathbf{d}(\mathbf{p})$. It was the principle contribution of Lewenstein [61] to thus recognise that the integral over \mathbf{p} is dominated by the region around the momentum \mathbf{p}_s for which the action is stationary, that is

$$\nabla_{\mathbf{p}} S_{\mathbf{p}}(t, t') \Big|_{\mathbf{p}=\mathbf{p}_s} = 0 \quad (3.65)$$

Substituting in $S_{\mathbf{p}}(t, t')$ from equation 3.58 and rearranging for \mathbf{p}_s then gives

$$\mathbf{p}_s(t, t') = -\frac{1}{\delta t} \int_{t'}^t \mathbf{A}(t'') dt'' \quad (3.66)$$

where $\delta t = t - t'$. If $\delta \mathbf{p} = \mathbf{p} - \mathbf{p}_s$, when expressed in Cartesian coordinates the Taylor expansion of $S_{\mathbf{p}}(t, t')$ about \mathbf{p}_s is then

$$\begin{aligned} S_{\mathbf{p}}(t, t') &= S_{\mathbf{p}_s}(t, t') + \sum_{j=1}^3 \frac{\partial S_{\mathbf{p}}}{\partial p_j} \Big|_{\delta p_j=0} \delta p_j + \frac{1}{2} \sum_{j,k=1}^3 \frac{\partial^2 S_{\mathbf{p}}}{\partial p_j \partial p_k} \Big|_{\delta p_{j,k}=0} \delta p_j \delta p_k + \dots \\ &\simeq S_{\mathbf{p}_s}(t, t') + \frac{\delta t}{2} \sum_{j=1}^3 \delta p_j^2 \end{aligned} \quad (3.67)$$

where the first-order term vanishes by equation 3.65 and from equation 3.58 it is seen that

$$\sum_{j,k=1}^3 \frac{\partial^2 S_{\mathbf{p}}}{\partial p_j \partial p_k} \Big|_{\delta p_{j,k}=0} = \begin{cases} \delta t & \text{if } j = k \\ 0 & \text{if } j \neq k \end{cases} \quad (3.68)$$

We may apply the approximate expression for $S_{\mathbf{p}}(t, t')$ to equation 3.57, simplifying the momentum integral to a saddle-point integral about \mathbf{p}_s . Furthermore, since $\mathbf{d}(\mathbf{p})$ varies much more slowly than $S_{\mathbf{p}}(t, t')$, we may take the DTMEs as constant over this region.

$$\begin{aligned} \int_{\mathbf{p}} \mathbf{d}^*(\mathbf{p} + \mathbf{A}(t)) \mathbf{d}(\mathbf{p} + \mathbf{A}(t')) e^{-iS_{\mathbf{p}}(t, t')} d^3 \mathbf{p} &\simeq \mathbf{d}^*(\mathbf{p}_s + \mathbf{A}(t)) \mathbf{d}(\mathbf{p}_s + \mathbf{A}(t')) e^{-iS_{\mathbf{p}_s}(t, t')} \int_{\mathbf{p}} e^{-\frac{i}{2} \delta t \delta \mathbf{p}^2} d^3 \mathbf{p} \\ &= \left(\frac{2\pi}{i\delta t} \right)^{\frac{3}{2}} \mathbf{d}^*(\mathbf{p}_s + \mathbf{A}(t)) \mathbf{d}(\mathbf{p}_s + \mathbf{A}(t')) e^{-iS_{\mathbf{p}_s}(t, t')} \end{aligned} \quad (3.69)$$

Performing this saddle-point integration is typically known as the *Saddle-Point Approximation* (SPA) and when applied to equation 3.57 yields

$$\mathcal{D}_s(t) = -i \int_{-\infty}^t \left(\frac{2\pi}{\varepsilon + i\delta t} \right)^{\frac{3}{2}} a^*(t) \mathbf{d}^*(\mathbf{p}_s + \mathbf{A}(t)) a(t') \mathbf{E}(t') \cdot \mathbf{d}(\mathbf{p}_s + \mathbf{A}(t')) e^{-iS_{\mathbf{p}_s}(t, t')} dt' + c.c. \quad (3.70)$$

This expression is greatly simplified over equation 3.57 and may be easily performed over a densely discretised temporal range. The physical interpretation remains as previously and the additional prefactor $\left(\frac{2\pi}{\varepsilon+i\delta t}\right)^{\frac{3}{2}}$ may be interpreted as describing the spreading of the wavepacket in while in the continuum, progressively reducing the contribution to $\mathcal{D}_s(t)$ with increasing δt . ε is a small, positive parameter introduced to the denominator to avoid a singularity when $\delta t = 0$.

Likewise, applying the SPA to equation 3.61 yields for the spectral amplitude of the dipole acceleration along $\hat{\mathbf{e}}$

$$M_{\hat{\mathbf{e}}}(\omega) = \frac{i\omega^2}{\sqrt{2\pi}} \int_{-\infty}^{\infty} \int_{-\infty}^t \left(\frac{2\pi}{\varepsilon+i\delta t}\right)^{\frac{3}{2}} a^*(t) \hat{\mathbf{e}} \cdot \mathbf{d}^*(\mathbf{p}_s + \mathbf{A}(t)) \\ \times a(t') \mathbf{E}(t') \cdot \mathbf{d}(\mathbf{p}_s + \mathbf{A}(t')) e^{-iS_{\mathbf{p}_s, \omega}(t, t')} dt' dt + c.c. \quad (3.71)$$

This is the equation which is implemented in our SFA-based single-atom HHG code.

3.3.5 The quantum orbit model

The quantum orbit (QO) model is a refinement of the SFA model of §3.3.4, where equation 3.71 is reduced to a sum over individual *Quantum Orbits*. These are paths comprised of frequency-dependent triplets $(\mathbf{p}_s, t_s, t'_s)$, where the action is stationary with respect to changes in all three variables, i.e.

$$\nabla S_{\mathbf{p}, \omega}(t, t') = 0 \quad (3.72)$$

Since the contributions of other paths to the dipole response quickly vanish away from these saddle-points, we may include their contribution via a Gaussian integration [68, 69].

Solving equation 3.72 yields the following three saddle-point equations

$$\mathbf{p}(t - t') = - \int_{t'}^t \mathbf{A}(t'') dt'' \quad (3.73)$$

$$(\mathbf{p} + \mathbf{A}(t))^2 = 2(\omega - I_p) \quad (3.74)$$

$$(\mathbf{p} + \mathbf{A}(t'))^2 = -2I_p \quad (3.75)$$

representing momentum conservation in the continuum, energy conservation during ionisation and energy conservation during recombination. Since equation 3.75 has no real solution for $I_p > 0$, we find the saddle-point solutions are necessarily complex, with $\text{Im}(t')$ serving as a definition of tunnelling time [70]. Before the saddle-point integration may be performed, the contour of integration must therefore be deformed into the complex plane to pass through each of the saddle-points. This is permitted since the integral is path-independent. Furthermore, complex time requires also that each of E , A , $\int A$ and

$\int A^2$ be defined over the complex plane. Computational limitations then require analytical expressions for each of these functions, restricting us to using \cos^2 envelopes (see §2.3.2).

We may Taylor expand $S_{\mathbf{p},\omega}(t, t')$ about t_s and t'_s (giving us \mathbf{p}_s according to equation 3.66) as

$$\begin{aligned} S_{\mathbf{p},\omega}(t, t') = S_{\mathbf{p}_s,\omega}(t_s, t'_s) &+ \frac{1}{2} \left(\left. \frac{\partial^2 S_{\mathbf{p},\omega}(t, t')}{\partial t^2} \right|_{\delta t=0} \delta t^2 + \left. \frac{\partial^2 S_{\mathbf{p},\omega}(t, t')}{\partial t'^2} \right|_{\delta t'=0} \delta t'^2 \right) \\ &+ \left. \frac{\partial^2 S_{\mathbf{p},\omega}(t, t')}{\partial t \partial t'} \right|_{\delta t, \delta t'=0} \delta t \delta t' \end{aligned} \quad (3.76)$$

where as before the first-order terms vanish according to 3.72 and we truncate to second-order. Substituting equation 3.76 into equation 3.71 gives amplitude for the emission of a photon of frequency ω from the quantum orbit defined by the saddle-point s as

$$\begin{aligned} \mathcal{Q}_s(\omega) &\simeq \frac{i2\pi\omega^2}{(\varepsilon + i\delta t_s)^{\frac{3}{2}}} a^*(t_s) \hat{\mathbf{e}} \cdot \mathbf{d}^*(\mathbf{p}_s + \mathbf{A}(t_s)) a(t'_s) \mathbf{E}(t'_s) \cdot \mathbf{d}(\mathbf{p}_s + \mathbf{A}(t'_s)) e^{-iS_{\mathbf{p}_s,\omega}(t_s, t'_s)} \\ &\times \int_{-\infty}^{\infty} \int_{-\infty}^t e^{-\frac{i}{2}\delta t^2 \left. \frac{\partial^2 S_{\mathbf{p},\omega}(t, t')}{\partial t^2} \right|_{\delta t=0} - \frac{i}{2}\delta t'^2 \left. \frac{\partial^2 S_{\mathbf{p},\omega}(t, t')}{\partial t'^2} \right|_{\delta t'=0} - i\delta t \delta t' \left. \frac{\partial^2 S_{\mathbf{p},\omega}(t, t')}{\partial t \partial t'} \right|_{\delta t, \delta t'=0}} dt' dt + c.c. \\ &= \frac{i2(\pi\omega)^2}{\sqrt{(\varepsilon + i\delta t_s)^3 \det H(S_{\mathbf{p},\omega})|_{\delta t, \delta t'=0}}} a^*(t_s) \hat{\mathbf{e}} \cdot \mathbf{d}^*(\mathbf{p}_s + \mathbf{A}(t_s)) \\ &\times a(t'_s) \mathbf{E}(t'_s) \cdot \mathbf{d}(\mathbf{p}_s + \mathbf{A}(t'_s)) e^{-iS_{\mathbf{p}_s,\omega}(t_s, t'_s)} + c.c. \end{aligned} \quad (3.77)$$

where $\delta t_s = t_s - t'_s$ and the Hessian matrix $H(S_{\mathbf{p},\omega})$ is given by

$$H(S_{\mathbf{p},\omega}) = \begin{pmatrix} \frac{\partial^2 S_{\mathbf{p},\omega}(t, t')}{\partial t^2} & \frac{\partial^2 S_{\mathbf{p},\omega}(t, t')}{\partial t \partial t'} \\ \frac{\partial^2 S_{\mathbf{p},\omega}(t, t')}{\partial t' \partial t} & \frac{\partial^2 S_{\mathbf{p},\omega}(t, t')}{\partial t'^2} \end{pmatrix} \quad (3.78)$$

The total HHG spectrum projected along an axis $\hat{\mathbf{e}}$ is then closely approximated by a coherent sum over these dominate quantum orbits, i.e.

$$M_{\hat{\mathbf{e}}}(\omega) = \sum_s \mathcal{Q}_s(\omega) \cdot \hat{\mathbf{e}} \quad (3.79)$$

Comparing equations 3.64 and 3.75 shows that the DTME $\mathbf{d}(\mathbf{p}_s + \mathbf{A}(t'_s))$ gives a singularity in the case of a 1s orbital. This is in fact the case for all orbitals so we therefore set this DTME to unity to perform the calculation. Since equation 3.75 holds equally for all quantum paths, this only serves to multiply the entire HHG spectrum by a constant. The correct absolute values may be obtained by comparing with the TDSE method.

While equations 3.77 and 3.79 imply a level of complexity less than that of the

SFA method, there are a number of complications in identifying and characterising the quantum orbit contributions. A full description is, for example, given in references [69] and [71]. Below we give an outline of the method employed.

At energies above the classical cut-off, $\omega > \mathcal{E}_c$, the amplitudes $\mathcal{Q}_s(\omega)$ drop off exponentially. However, the saddle-point solutions, s , do exist for all energies, tending to predictable and well-separated values above \mathcal{E}_c . For this reason the saddle-points are located first at an initial energy $\omega_i \gg \mathcal{E}_c$ using the method of steepest descent to improve upon educated initial guesses. Each saddle-point $s(\omega_i)$ is then used as the initial guess for $s(\omega_i - \delta\omega)$, which will lie close to $s(\omega_i)$ for small $\delta\omega$. In such a way the saddle-points are calculated for ω decreasing to zero, forming a set of continuous quantum paths.

The quantum orbits may be classified according to three types: (i) low-energy orbits, contributing to the HHG spectrum at energies $< I_p$, (ii) high-energy short orbits, principally contributing towards energies $> I_p$ and with ω increasing with travel time δt_s and (iii) high-energy long orbits, also contributing principally towards energies $> I_p$ but with ω decreasing with δt_s . The short and long high-energy paths describe the short and long trajectories introduced in §3.3.2.

Let us consider an electron ionised from a single half-cycle of the laser field. There is a single low-energy quantum orbit associated with this event, recolliding less than a quarter of a cycle later. There are, however, numerous pairs of subsequent short and long high-energy orbits, with the exact number dictated by the number of cycles in the pulse. The first pair recombine less than one full-cycle after ionisation, with each subsequent pair recombining within one-half cycle of the previous. These pairs are distinguished by colour in figure 3.7, which shows the first 13 quantum orbit solutions for an electron ionised from the half-cycle preceding the envelope peak of an 800 nm, 3 cycle pulse of $5 \times 10^{14} \text{ Wcm}^{-2}$ and $\phi_0 = 0$. The laser field during ionisation and recollision is also plotted in the top panes.

Each quantum orbit solutions is given a label α, β, m in accordance with the notation of references [69] and [72]. The label α distinguishes between the low-energy (0), short (+1) and long (-1) orbits. In figure 3.7, $\alpha = 0$ corresponds to the grey orbit and $\alpha = -1/+1$ corresponds to the rising/falling edges of the coloured high-energy pairs in pane (a) and vice versa in pane (b). The label β distinguishes between odd (-1) orbits, where $(n - \frac{1}{2})T \leq \delta t_s \leq nT$ for $n \in \mathbb{Z}$, from the even (+1) orbits, where $(n - 1)T \leq \delta t_s \leq (n - \frac{1}{2})T$. This distinction is important because, as is seen in figure 3.7, a given odd orbits will typically result in higher cut-off energies than the preceding even orbit, although this feature is diminished here due to the short pulse envelope. For a many cycle-pulse the odd / even orbits will converge in energy to $\omega = I_p + 2U_p$ from above / below with increasing δt_s [69]. The final label m measures δt_s directly as $m = \lfloor \frac{2\delta t_s}{T} \rfloor$, where $\lfloor \cdot \rfloor$ denotes greatest integer less than the argument. Note that this differs from

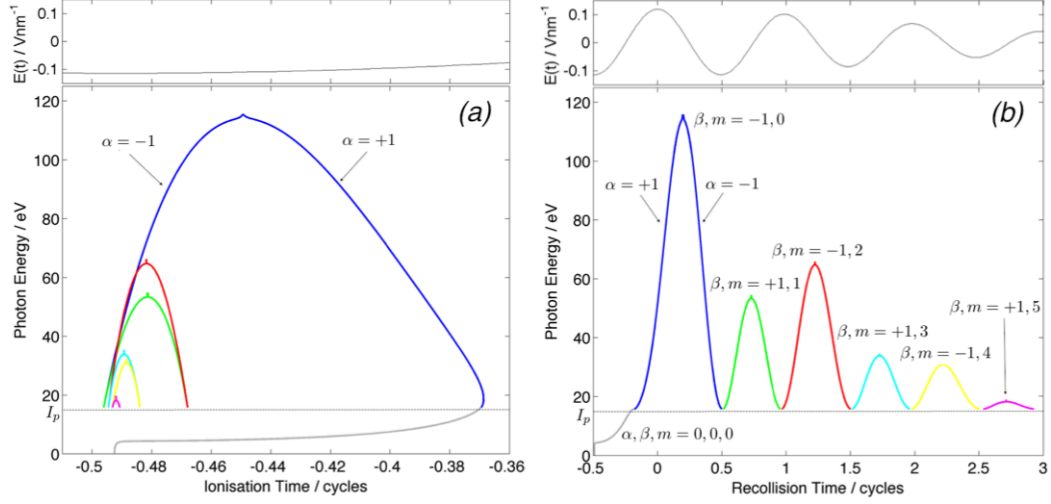


Figure 3.7: (a) Ionisation time and (b) recollision time plotted against emitted photon energy for the first 13 quantum orbit solutions ionised from the half-cycle preceding the envelope peak of an 800 nm, 3 cycle pulse of $5 \times 10^{14} \text{ Wcm}^{-2}$ and $\phi_0 = 0$. The low-energy orbit ($< I_p$) is plotted in grey and the high-energy orbit pairs coloured according to the label m . The vanishing contributions are killed off at energies exceeding the cut-off for each half-cycle. The driving pulse at these times is also plotted in the top panes.

the aforementioned references in that they considered multiples of full- rather than half-cycles. In figure 3.7 the orbits are coloured according to m , as labelled in pane (b).

One of the complications alluded to above arises from the existence of avoided crossings in the complex time plane between the quantum orbits. Considering only the $m = 0$ paths, we see two avoided crossings. The first resides at $\omega = I_p$ between the low-energy and short orbit. The second resides close to the classical cut-off $\omega = \mathcal{E}_c$ with an avoided crossing between the short and long high-energy orbits. For this reason, care must be taken we calculating the quantum paths by the method described above. It must be ensured that $\delta\omega$ is sufficiently small near the avoided crossings to prevent jumps between the two paths.

At the cut-off avoided crossing, the two orbits first pass through the so-called *Stokes Transition*, satisfying

$$\text{Re}\{S_\omega^{(short)}(t_s, t'_s)\} = \text{Re}\{S_\omega^{(long)}(t_s, t'_s)\} \quad (3.80)$$

where we have dropped the subscript \mathbf{p}_s on the action (unnecessary by equation 3.66).

After this transition, the orbit with the larger imaginary component will begin to diverge. At slightly higher energy the *Anti-Stokes Transition* is reached, which satisfies

$$\text{Im}\{S_\omega^{(short)}(t_s, t'_s)\} = \text{Im}\{S_\omega^{(long)}(t_s, t'_s)\} \quad (3.81)$$

and by this point the diverging solution may not be reached by the method of steepest descent and must be discarded [73]. This rejection results in inaccurate results near the cut-off. These difficulties may be overcome, however, by taking instead the *Uniform Approximation* (UA) [69, 73]. Here the paths of equal m are combined in an asymptotic expansion for $\mathcal{Q}_{\beta,m}(\omega)$, where we have replaced the subscript s with the characteristic labels β and $m > 0$. For $\omega > I_p$, $\mathcal{Q}_{\beta,m}(\omega)$ is approximated as [69]

$$\mathcal{Q}_{\beta,m}(\omega) = \zeta \sqrt{6\pi S_-} e^{i(S_+ + \frac{\pi}{4})} \left(\frac{A_-}{\sqrt{z}} \text{Ai}(-z) + i \frac{A_+}{z} \text{Ai}'(-z) \right) \quad (3.82)$$

for the parameters

$$S_{\pm} = \frac{1}{2} \left(S_{\omega}^{+1,\beta,m} \pm S_{\omega}^{-1,\beta,m} \right) \quad (3.83)$$

$$A_{\pm} = \frac{1}{2} \left(A_{\omega}^{+1,\beta,m} \pm i A_{\omega}^{-1,\beta,m} \right) \quad (3.84)$$

$$z = \begin{cases} \left(\frac{3S_-}{2} \right)^{\frac{2}{3}} & \text{if } \omega < \mathcal{E}_{AS} \\ \left(\frac{3S_-}{2} \right)^{\frac{2}{3}} e^{\frac{i2\pi\beta}{3}} & \text{if } \omega > \mathcal{E}_{AS} \end{cases} \quad (3.85)$$

$$\zeta = \begin{cases} +1 & \text{if } \omega < \mathcal{E}_{AS} \\ -1 & \text{if } \omega > \mathcal{E}_{AS} \end{cases} \quad (3.86)$$

with \mathcal{E}_{AS} denoting the energy at which the anti-Stokes transition occurs. Ai and Ai' denote the complex Airy function and its derivative [74]. Note that the amplitude of the $m = 0$ orbit triplet requires the addition of the contribution of the low-energy orbit to equation 3.82.

While the UA allows for greater accuracy at the cut-off, it sums orbits over α (coupling the short- and long-orbit pairs) and so is only used when they are not required separately. In this case the SPA is invoked with the non-diverging saddle-point used as a first approximation to the cut-off region for both short and long orbits.

Conversely to the example of figure 3.7, and typically of greater interest in HHG, is to examine the set of quantum orbits which recombine within a specific half-cycle. This allows us to separate out the various half-cycle contributions and determine the degree to which each contributes to the total HHG spectrum. Figure 3.8 shows the first 13 quantum orbit solutions recolliding during the half-cycle at the envelope peak of the same laser pulse as in figure 3.7. As previously the orbits are coloured according to m and are now labelled with respect to the half-cycle of recollision. We see that the $m = 0$ orbits triplet is spread across the entire half-cycle, with the low-energy trajectory occupying approximately the first third and the high-energy pair the remainder. By contrast, for $m > 0$ the orbit pairs are all localised into the second half of the half-cycle. From figure

3.8 (a) we see that the odd and even orbits possess cut-off energies clearly approaching $I_p + 2U_p$ from above and below, respectively, with increasing δt_s .

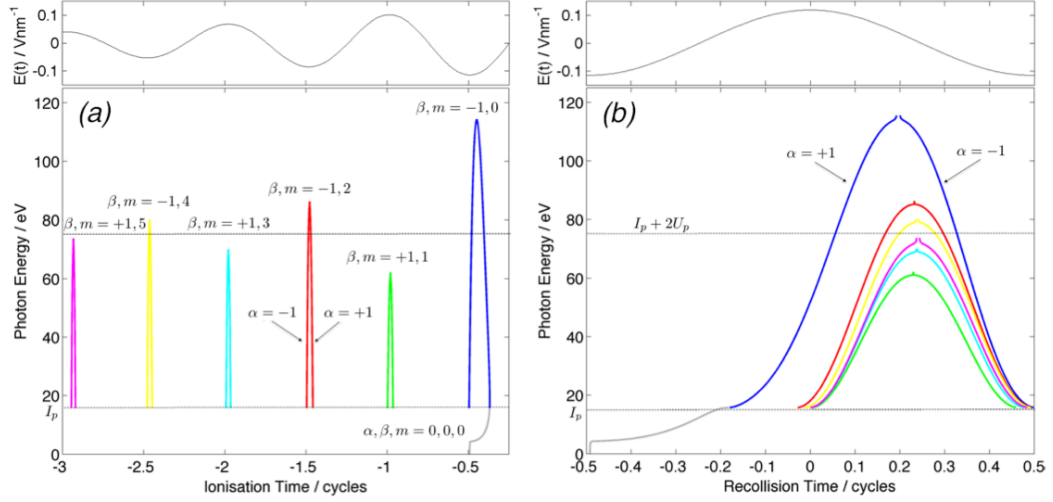


Figure 3.8: (a) Ionisation time and (b) recollision time plotted against emitted photon energy for the first 13 quantum orbit solutions recombining during the half-cycle across the envelope peak of an 800 nm, 3 cycle pulse of $5 \times 10^{14} \text{ Wcm}^{-2}$ and $\phi_0 = 0$. The orbits are labelled and coloured as in figure 3.7 and are again killed off above the cut-off of each half-cycle. The individual half-cycle cut-off energies are seen to converge to $I_p + 2U_p$ with increasing δt_s . The driving pulse is also plotted in the top panes.

We may then use these quantum orbit solutions to calculate the photoelectron spectrum arising from each of the orbits in turn. Figure 3.9(a) plots the spectra of the short (bold) and long (dashed) high-energy orbits, calculated using the SPA via equation 3.77 and coloured as in figure 3.8. The short orbits are seen to be typically of greater intensity than the long, with both dropping with increasing δt_s . Further away from the envelope peak this may be by as much as two orders of magnitude between half-cycles in this case. The half-cycle cut-off energies are again seen to converge to $I_p + 2U_p$ (dashed black line) from above for $\beta = -1$ and below for $\beta = +1$. As previously noted, the intensity near the cut-off is inaccurate with the SPA, manifesting as raised peaks in this plot.

Figure 3.9(b) instead invokes the UA, coupling the short and long orbits within each half-cycle to produce uniformly accurate half-cycle spectra. Again the spectra are coloured to match with figure 3.8. As expected, the phase difference between the short and long orbits is seen to decrease with increasing photon energy, corresponding to a decreasing difference in excursion duration between the two orbits.

Figure 3.9(c) plots the total photon spectrum for this half-cycle (0) as a black line, obtained from a coherent sum over the spectra of figure 3.9(b). The orbit pairs $m = 0$ and, for $\mathcal{E} \lesssim 60 \text{ eV}$, $m = 1$ are seen to dominate the half-cycle spectrum. A small

contribution from the pair $m = 2$ is also seen. Also plotted for comparison in pale blue and green are the half-cycle spectra from the preceding (-1) and succeeding (+1) half-cycles respectively.

Figure 3.9(d) plots the full HHG spectrum across the entire pulse, calculated as a coherent sum across all half-cycle spectra.

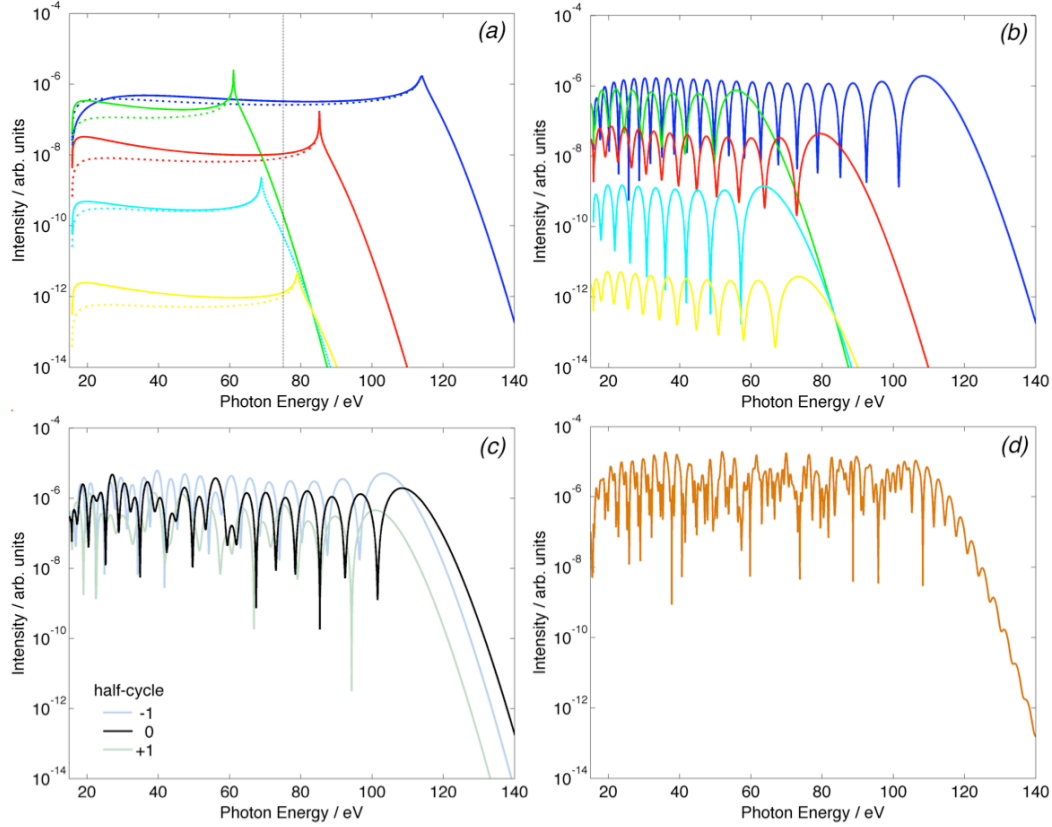


Figure 3.9: (a) Short (bold) and long (dashed) orbit spectra calculated using the SPA for a driving pulse of figure 3.8 using the same colour-labelling, with the half-cycle cut-offs approaching the limit of $I_p + 2U_P$ (vertical dashed line). (b) Corresponding orbit pair spectra calculated using the UA. (c) Summed half-cycle spectra for recombination during the three central half-cycles and (d) the full HHG spectra across the entire pulse.

3.3.6 Wavelet analysis

The harmonic spectrum as recorded in the laboratory is integrated over a timescale much longer than any single pulse. These data are thus typically recorded as an intensity spectrum via an MCP (see §3.2) and analysed solely in the frequency domain. To compare the experimental results with theory we may simply Fourier transform the dipole moment or acceleration as calculated via any of the above methods.